minerals

MDPI

Article

An Improved Understanding of Chalcopyrite Leaching Mechanisms: The Influence of Anisotropic Crystal Planes

Zhenlun Wei [1], Xu Yang [1], Wanqing Li [1], Qiang Ma [1], Xiaoyong Wu [1] and Yubiao Li [1,2,*]

[1] School of Resources and Environmental Engineering, Wuhan University of Technology, Wuhan 430070, China; erebus@whut.edu.cn (Z.W.); xuyang@whut.edu.cn (X.Y.); wanqing.li@whut.edu.cn (W.L.); qiang.ma@whut.edu.cn (Q.M.); parawu521@163.com (X.W.)

[2] Key Laboratory of Green Utilization of Critical Non-Metallic Mineral Resources, Ministry of Education, Wuhan University of Technology, Wuhan 430070, China

* Correspondence: yubiao.li@whut.edu.cn

Abstract: Chalcopyrite ($CuFeS_2$) particles, exposing anisotropic crystal planes during the grinding process, possess comprehensive surface properties that affect their leaching behaviors. In order to investigate the influence of anisotropic crystal planes on the leaching mechanisms, $CuFeS_2$ particles with anisotropic crystal planes were produced by employing three-head laboratory grinder mill (TM), rod mill (RM), and ball mill (BM) and were then leached in a sulfuric acid solution at pH = 1. Based on the XRD, SEM, XPS, and simulation results, (112), (102), (312), (110), (116), (100), and (001) planes were mainly exposed on the $CuFeS_2$ surface during the crushing and grinding process. In addition, fewer (112), (102), (312), and (110) planes but more (116), (100), and (001) planes were exposed on the $CuFeS_2$ samples in the TM method than in the RM and BM methods. Since the leaching rates were in the order of (001) > (100) > (116) > (110) > (312) > (102) > (112) planes, the Cu extractions followed an order of TM > RM > BM. This study, therefore, provides an excellent theoretical basis for the effect of anisotropic crystal planes on $CuFeS_2$ leaching, further improving the understanding of $CuFeS_2$ leaching mechanisms.

Keywords: chalcopyrite; leaching; anisotropic crystal planes; density functional theory; mechanisms

Citation: Wei, Z.; Yang, X.; Li, W.; Ma, Q.; Wu, X.; Li, Y. An Improved Understanding of Chalcopyrite Leaching Mechanisms: The Influence of Anisotropic Crystal Planes. *Minerals* **2023**, *13*, 1461. https://doi.org/10.3390/min13111461

Academic Editor: Przemyslaw B. Kowalczuk

Received: 13 October 2023
Revised: 5 November 2023
Accepted: 14 November 2023
Published: 20 November 2023

1. Introduction

Copper is an important nonferrous metal that has been widely used in various areas such as the light, electrical, communications, construction, and machinery manufacturing industries and other industries [1]. Copper metal is mainly purified from chalcopyrite ($CuFeS_2$), since approximately 70% of the Earth's copper resources are found as $CuFeS_2$ [2,3]. The average copper grades are about 0.4% and 1~2% for open-cast and underground $CuFeS_2$ deposits [1], respectively. Generally, a flotation process is employed to obtain a $CuFeS_2$ concentrate [4], followed by the metallurgy process for copper production [5]. In addition, pyrometallurgical methods are preferentially considered for high-grade $CuFeS_2$ concentrates (greater than 20%) [6]. However, these methods lead to extensive environmental problems due to the emission of SO_2 [7,8]. As an alternative to pyrometallurgy, hydrometallurgy has been paid much attention due to its advantages, such as being a more economical method of treating low-grade ores and being more environmentally friendly [3,5].

However, hydrometallurgical processing of $CuFeS_2$ has not been widely adopted in the industry due to the extremely slow leaching kinetics [9–14], mainly due to the formation of passivation layers on the $CuFeS_2$ surface [15–21]. Thus, the investigation of the formation and elimination mechanisms of the passivation layer is very important for the application of $CuFeS_2$ hydrometallurgy. In recent years, various analytical methods have been applied to investigate the properties of the passivating layer on the $CuFeS_2$ surface [22–25], such as scanning electron microscopy (SEM), synchrotron scanning photoelectron microscopy (SPEM), transmission electron microscopy (TEM), and X-ray photoelectron spectroscopy

(XPS). However, there is no generally accepted theory as to the composition of the passivation layer. Córdoba et al. [3] reported that the passivation layers were predominantly composed of bimetallic sulfide, iron-deficient copper polysulfide, and elemental sulfide. Li et al. [5] reported that the formation of elemental sulfide, disulfide, polysulfide, and iron hydroxy-oxide inhibited the leaching of $CuFeS_2$. In this case, it is extremely urgent to clarify the surface properties of $CuFeS_2$ to better understand the leaching mechanisms.

In addition, the surface properties of minerals are closely associated with the mineral's exposed planes. For instance, Wei et al. [26] indicated that the MoS_2 face (i.e., (001) plane) exhibited hydrophobic properties while the MoS_2 edges (i.e., (103), (105), (100), and (110) planes) exhibited hydrophilic properties. Therefore, investigations on the anisotropic crystal planes are very important for determining the surface properties of $CuFeS_2$. Normally, the $CuFeS_2$ (112), (102), (312), (110), (116), (100), and (001) planes are exposed during the crushing and grinding process [27–30]. The properties of these crystal planes have been widely investigated using density functional theory (DFT) calculations from the viewpoint of theory. For example, de Oliveira et al. [31] reported three different reconstruction mechanisms for $CuFeS_2$-typical planes, wherein the reconstructed planes presented different properties. Wei et al. [27] investigated the relaxation and oxidation of the $CuFeS_2$ (001) and (112) planes on exposure to O_2 and H_2O, indicating that the formation of disulfide (S_2^{2-}) on the $CuFeS_2$ (001) plane and polysulfide (S_n^{2-}) on the $CuFeS_2$ (112) plane inhibited the leaching process. Meanwhile, the $CuFeS_2$ (001) plane per unit area was more easily oxidized than the (112) plane. However, the influence of the anisotropic crystal planes' properties on the actual leaching performance of $CuFeS_2$ and the underlying mechanisms remain unclear up to now.

In this study, three different grinding methods (i.e., a three-head laboratory mill with a grinder mill (TM), a rod mill (RM), and a ball mill (BM) were considered to obtain $CuFeS_2$ particles with anisotropic crystal planes, followed by the leaching experiment to investigate the influence of the anisotropic crystal plane on the leaching behavior of $CuFeS_2$. The anisotropy of the $CuFeS_2$ raw samples was analyzed using X-ray diffraction (XRD) and SEM; XPS and DFT simulation were employed to investigate the anisotropic oxidation properties of the $CuFeS_2$ planes. This study, therefore, provides an excellent theoretical basis in revealing the influence of anisotropic crystal planes on $CuFeS_2$ leaching mechanisms, providing new insights for the application of $CuFeS_2$ hydrometallurgy.

2. Materials and Methodology

2.1. $CuFeS_2$ Samples

The high-purity chunks of $CuFeS_2$ samples (Figure S1 and Table S1, Supplementary Materials, the content of $CuFeS_2$ was nearly 98 wt%) obtained from the Araci Mine in Peru were crushed to small particles (around 5 mm) and milled in three ways, i.e., TM (RK/XPM 120 × 3 three-head grinding machine, Wuhan Rock Grinding Equipment Manufacturing Co., Ltd., Wuhan, China), RM (XMB-70, three-roller, four-barrel rod mill, Wuhan Prospecting Machinery Factory, Wuhan, China), and BM (XMB-70, three-roller, four-barrel ball mill, grinding mediums using ceramic balls), followed by wet sieving to obtain particles with two size fractions of 38~75 μm and 75~150 μm. These samples were treated using ultrasonication (JP-020, Shenzhen Jie Meng Cleaning Equipment Co., Ltd, Shenzhen China) under ethanol solution conditions at 40 KHz for 2 mins to remove the attached fine particles from the sample surfaces, which were freeze-dried (LGJ-12, vacuum freeze dryer, Beijing Songyuanhuaxing Technology Develop Co., Ltd., Beijing, China) to avoid further surface oxidation.

2.2. Leaching Experiments

Briefly, 500 mL glass reactor vessels with a 5-port lid were used for the leaching experiments. A 1 g $CuFeS_2$ sample and 400 mL of a sulfuric acid solution at pH = 1 were poured into the reactor vessel to avoid interference from other ions [5] and were then heated using a thermostatically controlled silicone oil bath at 75 °C. The 5-port lid provided access

to the leach solution; three ports were used to house a thermometer, a Teflon impeller, and a reflux condenser, and the remaining two ports were covered with a plug to avoid moisture evaporation. The four-blade Teflon impeller was driven by a digitally controlled stirrer at a constant agitation speed of 170 rpm.

Subsequently, 5 mL solution samples were taken twice a day at intervals of 8 h and 16 h, respectively. Then, the solution was filtered through a 0.22 μm membrane for pH and Cu-concentration tests. The pH was maintained at 1 by adding 5 M H_2SO_4 [5].

2.3. Bulk and Surface Analyses

In order to determine the exposed crystal planes for the $CuFeS_2$ samples treated through the TM, RM and BM methods, $CuFeS_2$ samples with size fractions of 38~75 μm and 75~150 μm were directly tested using XRD (D8 Advance, Bruker, Germany, with 2θ from 10° to 70° (Cu Kα) at a scanning speed of 0.2°/min). The obtained data were analyzed using Jade 6.0 software (Materials Data, Inc., Livermore, CA, USA) to determine the exposed crystal planes corresponding to each diffraction peak based on the standard XRD pattern. Since the preferred orientation may exist in the XRD test for bigger $CuFeS_2$ particles, side-loading methods and the rotation of the sample table were considered to avoid the preferred orientation [32]. SEM analyses (Zeiss Ultra Plus, Oberkochen, Germany) were conducted on the surface of leached $CuFeS_2$, with an acceleration voltage of 30 keV.

A Thermo Scientific K-Alpha (Thermo Fisher-VG Scientific, Waltham, MA, USA) was used for XPS analyses of the leached $CuFeS_2$. The XPS instrument was operated using an Al K-Alpha X-ray source ($h\nu$ = 1486.6 eV) at 12 kV and 6 mA with a pressure of 2.0×10^{-7} m Bar. Next, 2.0 g of samples with a particle size of 38~75 μm were conditioned. The obtained spectra were analyzed using Avantage software (Thermo Fisher-VG Scientific, Thermo Fisher Scientific, Waltham, MA, USA). The binding energies were referenced to the C 1*s* peak at 284.8 eV.

2.4. DFT Calculation

The $CuFeS_2$ bulk was constructed through Materials Studio 8.0 according to our previous research [27]. The geometric optimization calculation was performed using the same calculation parameters, i.e., generalized gradient approximation (GGA) with PW91 corrections in the CASTEP package, with a cutoff energy of 351 eV, and a Monkhorst−Pack scheme with a $3 \times 3 \times 3$ *k*-point mesh. Subsequently, the $CuFeS_2$ (112), (102), (312), (110), (116), (100), and (001) planes were cleaved based on the optimized $CuFeS_2$ bulk. The surface energies (E_s) [27,33] and the adsorption energy [34] were calculated to determine the reactivity of the $CuFeS_2$ plane.

3. Results and Discussion

3.1. Anisotropic Leaching Results

In order to investigate the influence of the anisotropic crystal plane on $CuFeS_2$ leaching, three different grinding methods (TM, RM, and BM) were employed to obtain $CuFeS_2$ particles with anisotropic crystal planes, which were then leached in a H_2SO_4 solution. For the three $CuFeS_2$ samples with a particle size of 38~75 μm, a similar increasing trend of Cu extractions was obtained (Figure 1a), giving Cu extractions at around 76.2%, 78.9%, and 87.5% at 648 h for the TM, RM, and BM methods, respectively. In contrast, significantly different evolutions of Cu extractions were observed for the three $CuFeS_2$ samples with a particle size of 75~150 μm (Figure 1b), giving a Cu extraction order of TM > RM > BM. It should be noted that Cu was nearly completely extracted within 500 h for the TM method, while the Cu extractions were around 94% and 53% at 648 h for the RM and BM methods, suggesting that the TM method was beneficial for the leaching of bigger $CuFeS_2$ particles.

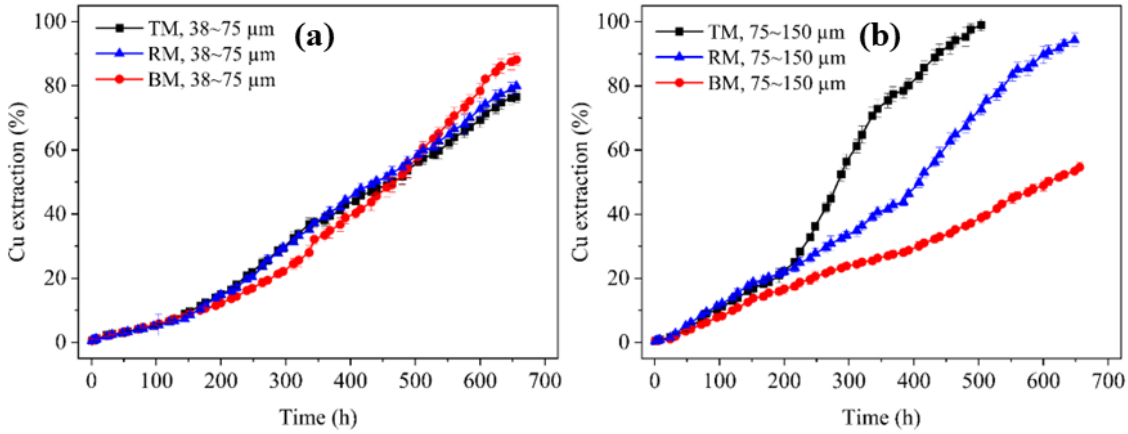

Figure 1. Leaching experiment results of $CuFeS_2$ samples obtained through three grinding methods: (**a**) 38~75 μm; (**b**) 75~150 μm.

In addition, the leaching rate was higher for smaller $CuFeS_2$ particles in the BM method due to their bigger surface area [5,35]. However, the bigger $CuFeS_2$ particles obtained through the TM and RM methods exhibited a higher leaching rate than the smaller particles, especially for the TM method, suggesting that the surface properties of the $CuFeS_2$ particles in the three grinding methods led to significantly different leaching results.

3.2. *Anisotropy of $CuFeS_2$ Raw Samples*

In order to investigate the differences in the surface properties, XRD and SEM tests were employed for the $CuFeS_2$ raw samples. Figure 2 shows the XRD patterns; the typical exposed planes for all the $CuFeS_2$ raw samples were the (112), (102), (312), (110), (116), (100), and (001) planes [27–30]. For the size fraction of 38~75 μm, all diffraction peaks at various planes of the three $CuFeS_2$ samples exhibited a similar intensity, suggesting that the exposed percentages of each plane for the three smaller $CuFeS_2$ particles were similar (Figure 2a), since the intensity of the diffraction peak is highly related to the exposed percentage of the planes [27,33,36]. In contrast, the intensities of diffraction peaks at various planes for the three $CuFeS_2$ samples with a particle size of 75~150 μm were significantly different (Figure 2b), suggesting that bigger $CuFeS_2$ particles from all three grinding methods had different exposed percentages for each plane, thus presenting different leaching rules as shown in Figure 1b. In other words, the anisotropic crystal planes of the $CuFeS_2$ particles seemed to dominate their leaching behavior.

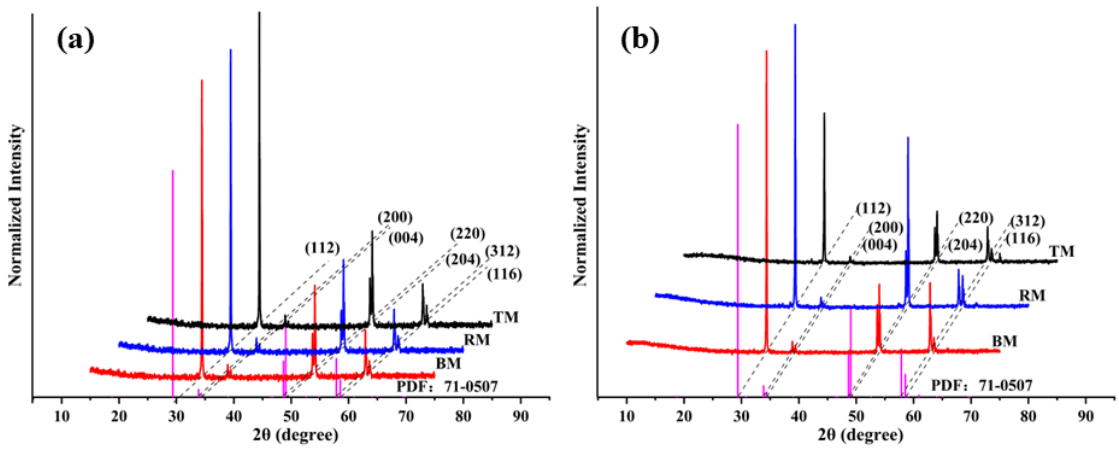

Figure 2. XRD patterns of raw $CuFeS_2$ samples obtained through three grinding methods: (**a**) 38~ 75 μm; (**b**) 75~150 μm. PDF: 71-0507 was the standard XRD pattern of $CuFeS_2$ from Jade 6.0.

In order to further investigate the anisotropy of the raw $CuFeS_2$ samples, the normalized percentages of the typically exposed planes for three $CuFeS_2$ samples based on the diffraction peak intensity of each plane were calculated (Figure 3 and Tables S2 and S3). Obviously, the normalized percentage rules of the (112), (102), (312), (110), (116), (100), and (001) planes for the three $CuFeS_2$ samples with particle sizes of 38~75 μm and 75~150 μm were different, e.g., the differences in the normalized percentages between the standard value and the experimental value of the (112) plane for the TM, RM, and BM methods were −9.279%, −8.210%, and −7.456% for the three smaller $CuFeS_2$ particles, while they were −15.357%, −13.541%, and −6.307% for the three bigger $CuFeS_2$ particles, respectively, indicating that the three bigger $CuFeS_2$ particles exhibited greater differences in their exposure percentages. For the (001) plane, the three smaller $CuFeS_2$ samples still exhibited similarly normalized percentages for the TM, RM, and BM methods (i.e., 3.856%, 3.908%, and 3.264%, respectively). However, the three bigger $CuFeS_2$ particles exhibited different normalized percentages of the exposed planes for the TM, RM, and BM methods (i.e., 3.613%, 2.959%, and 2.053%, respectively), suggesting that the three bigger $CuFeS_2$ particles exhibited greater anisotropy than the smaller $CuFeS_2$ particles. In addition, the total percentages of the (112), (102), and (312) planes for the three bigger $CuFeS_2$ particles were in the order of TM > RM > BM, while the (110), (116), (100), and (001) planes exhibited a total percentage order of TM < RM < BM (Figure 3), further demonstrating the crystal plane anisotropy for the three bigger $CuFeS_2$ particles.

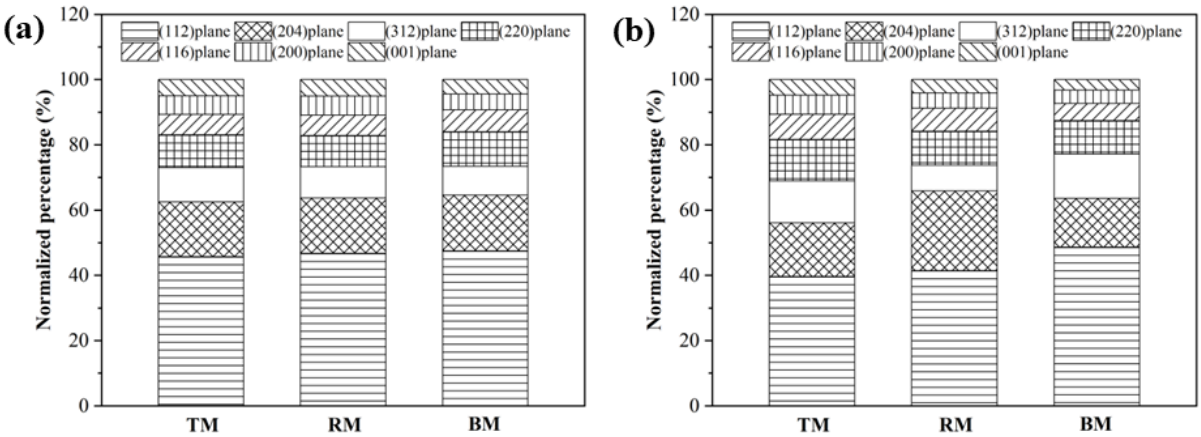

Figure 3. Normalized percentage of planes for three $CuFeS_2$ samples (%): (**a**) 38~75 μm; (**b**) 75~150 μm.

Figure 4 presents the SEM results of raw $CuFeS_2$ samples at 75~150 μm for the TM, RM, and BM methods. It can be clearly observed that the samples in the TM and RM methods were mainly long, irregular particles, while the samples in the BM method were mainly rounded particles. As shown in Table 1, the length–width ratios based on the average length and width for raw $CuFeS_2$ samples in the TM, RM, and BM methods were 1.776, 1.759, and 1.299, respectively, suggesting that the exposure percentage for each plane was related to the length–width ratio of the particles. Combining the normalized percentage of the typical exposed plane and the length–width ratio of the raw $CuFeS_2$ samples, the long, irregular particles in the TM method exposed fewer (112), (102), (312), and (110) planes but more (116), (100), and (001) planes than the rounded particles in the BM method.

Table 1. Average length, width, and length–width ratio for three raw $CuFeS_2$ samples.

Grinding Methods	Average Length (μm)	Average Width (μm)	Length–Width Ratio
TM	127.762	71.953	1.776
RM	124.724	70.917	1.759
BM	95.234	73.276	1.299

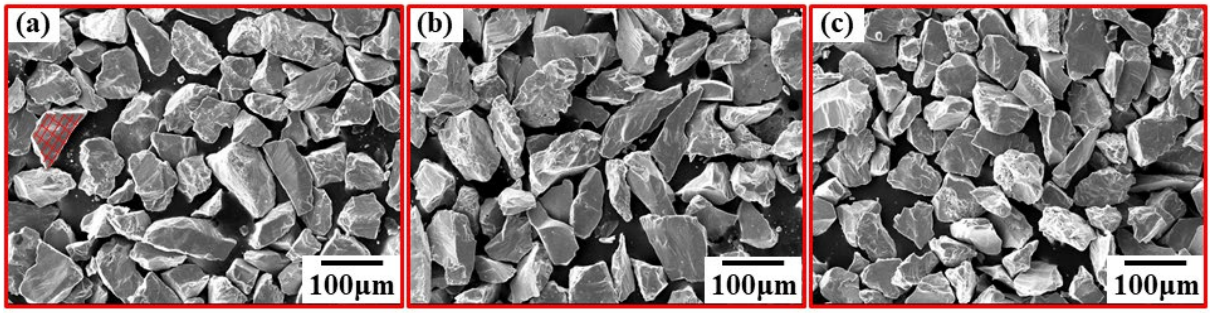

Figure 4. SEM images of raw $CuFeS_2$ samples (75~150 μm) obtained through three grinding methods: (**a**) TM; (**b**) RM; (**c**) BM. The average length and width of each raw $CuFeS_2$ sample was calculated based on 5 lengths and 5 widths as shown in (**a**) (the red lines), respectively.

3.3. XPS Analysis

The three bigger $CuFeS_2$ samples were tested using XPS to investigate the species differences on the $CuFeS_2$ surface. Figure 5 and Table 2 show the XPS survey spectra of the $CuFeS_2$ surface and the elemental quantification (at %) of the $CuFeS_2$ surfaces, respectively. The O 1*s* peak at 532.1 eV was found on the $CuFeS_2$ surface, and the O contents were 43.87%, 53.37%, and 70.40% on the surface of $CuFeS_2$ treated using the BM, RM, and TM methods, respectively, indicating that the order of the oxidation degree of the $CuFeS_2$ surface treated using different methods was TM > RM > BM.

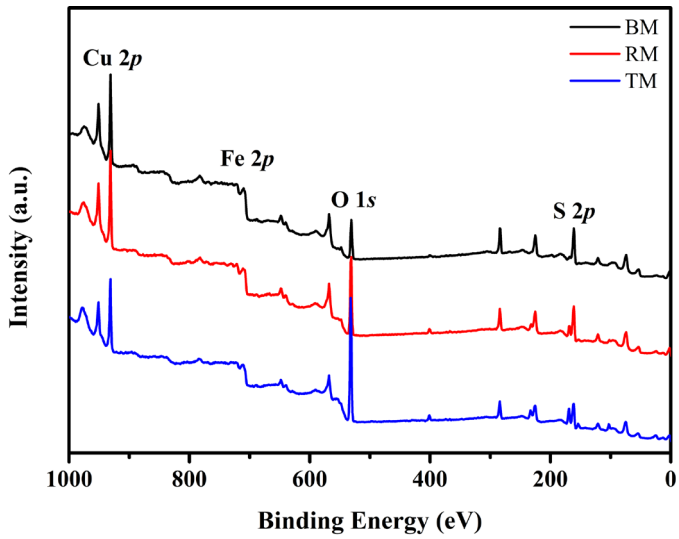

Figure 5. XPS survey spectra of $CuFeS_2$ treated using BM, RM, and TM.

Table 2. Elemental quantification (at %) of $CuFeS_2$ surface.

Element	Bonding Energy (eV)	$CuFeS_2$		
		BM	RM	TM
S 2*p*	161.4	9.26	4.93	8.08
O 1*s*	532.1	43.87	53.37	70.40
Fe 2*p*	710.8	8.56	9.48	4.88
Cu 2*p*	932.6	38.31	32.22	16.64

The Fe contents on the surface of $CuFeS_2$ treated using the BM, RM, and TM methods were determined to be 8.56%, 9.48%, and 4.88%, respectively, indicating that Fe was more readily leached from the surface of $CuFeS_2$ when treated with the TM method. The Cu contents on the surface of the $CuFeS_2$ treated using the BM, RM, and TM methods were

found to be 38.31%, 32.22%, and 16.64%, respectively, suggesting that Cu was more easily leached from the surface of $CuFeS_2$ when subjected to the TM method, compared with both the BM and RM methods. This observation is consistent with the leaching results presented in Figure 5.

Figure 6 and Table 3 show the fitted S 2*p* spectra and S species of the bigger $CuFeS_2$ particles treated using the BM, RM, and TM methods. The S $2p_{3/2}$ component located at 161.4 eV for $CuFeS_2$ was attributed to the monosulfide S^{2-} species [37,38]. The $2p_{3/2}$ spectra due to S_2^{2-}, S_n^{2-}, S^0, SO_3^{2-}, SO_4^{2-} and the energy loss of $CuFeS_2$ were located at 162.2, 163.2, 163.7, 166.3, 168.8, and 165.1 eV, respectively [38–40]. The concentrations of S_2^{2-}, S_n^{2-}, S^0, SO_3^{2-}, and SO_4^{2-} on the BM-treated $CuFeS_2$ surface were 8.60%, 0%, 23.57%, 3.81%, and 34.59%, respectively (Table 3). The presence of oxidized S species indicated that the surface S^{2-} of $CuFeS_2$ was oxidized to S_2^{2-}, S_n^{2-}, and S^0, which were the main substances forming the passivation layer [41]. The passivation layer composed of S_2^{2-}, S_n^{2-}, and especially S^0, hindered the further leaching of $CuFeS_2$, which was the main reason for the low leaching rate of $CuFeS_2$ treated using the BM method.

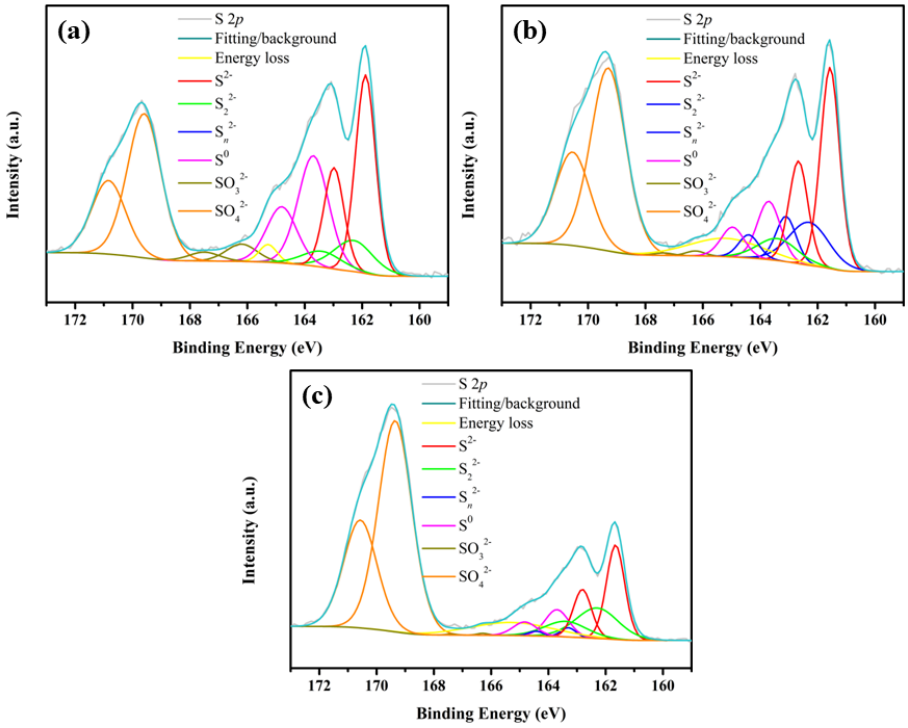

Figure 6. S 2*p* XPS spectra of $CuFeS_2$ treated using the (**a**) BM, (**b**) RM, and (**c**) TM methods.

Table 3. S species (at %) on $CuFeS_2$ surfaces treated under different conditions.

S Species	Bonding Energy (eV)	Full Width at Half-Maximum (eV)	$CuFeS_2$		
			BM	RM	TM
S^{2-}	161.4	0.7–0.8	27.98	23.01	14.87
S_2^{2-}	162.2	0.7–0.9	8.60	10.32	11.07
S_n^{2-}	163.2	1.1–1.3	0	5.50	1.19
S^0	163.7	1.0–1.2	23.57	8.12	5.44
SO_3^{2-}	166.3	1.1–1.3	3.81	0.54	0.20
SO_4^{2-}	168.8	1.5–1.6	34.59	39.02	61.14
Energy loss	165.1	1.4–1.7	1.46	5.37	6.10

The concentrations of S_2^{2-}, S_n^{2-}, S^0, SO_3^{2-}, and SO_4^{2-} on the RM-treated $CuFeS_2$ surface were 10.32%, 5.50%, 8.12%, 0.54%, and 39.02%, respectively (Table 3). The S species

content on the surface of $CuFeS_2$ treated using the TM method was comparable to that observed on the surface of $CuFeS_2$ treated using the RM method, except for a higher presence of SO_4^{2-} compounds. The low concentration of S^0 and the high concentration of SO_4^{2-} indicated that the surface of $CuFeS_2$ treated using the RM and TM methods had reduced passivation layer formation, enhancing the generation of highly oxidized SO_4^{2-} during leaching, further facilitating the leaching process. The highest SO_4^{2-} content was found on the $CuFeS_2$ surface treated using the TM method, indicating a significant oxidation reaction and the maximum leaching rate. Overall, the $CuFeS_2$ samples treated using the BM, RM, and TM methods in the same leaching conditions underwent varying degrees of oxidation, especially showing different evolutions for the S species on the chalcopyrite surface. These results indicate that the anisotropic crystal planes of $CuFeS_2$ significantly affected its leaching behavior.

3.4. The Properties of Anisotropic Crystal Planes

In order to further investigate the reactivities of $CuFeS_2$ planes, the properties of the $CuFeS_2$ planes were investigated through the same calculation methods as in our previous research (e.g., only Fe and S sites were considered for the adsorption of O_2) [27]. Due to the symmetry of the $CuFeS_2$ structure (i.e., each Cu/Fe atom is bonded with four surrounding S atoms, each S atom is bonded with two surrounding Cu atoms and two surrounding Fe atoms) [31], the $CuFeS_2$ (112), (312), (116), (100), and (001) planes exposed both sulfur-terminated (only exposing S atoms) and metal-terminated (only exposing Fe/Cu atoms) planes, while the $CuFeS_2$ (102) and (110) planes exposed mixed terminated (exposing both S and Fe/Cu atoms) planes during the cleavage process (Figure S2), which fully exhibited the anisotropic structure of $CuFeS_2$ planes.

Table 4 exhibits the surface energies of the $CuFeS_2$ planes, giving the order of (112)-S < (112)-M < (102) < (312)-M < (312)-S < (110) < (116)-S < (116)-M < (100)-S < (100)-M < (001)-S < (001)-M planes, suggesting that the stabilities of the $CuFeS_2$ planes were in the order of (112) > (102) > (312) > (110) > (116) > (100) > (001) planes [27,42–44], consistent with the exposed percentage of $CuFeS_2$ planes for all the grinding methods (Figure 3), e.g., the $CuFeS_2$ (112) plane obtained the lowest surface energy (0.923 $J \cdot m^{-2}$ for the (112)-S plane and 1.018 $J \cdot m^{-2}$ for the (112)-M plane) and was, thus, preferentially exposed during the grinding process [27], occupying the highest exposed percentage (more than 40%, Table S1). It should be noted that the $CuFeS_2$ (001) planes with the highest surface energy (1.495 $J \cdot m^{-2}$ for the (001)-S plane and 1.556 $J \cdot m^{-2}$ for the (001)-M plane) were less easily exposed during the grinding process, occupying the lowest exposed percentage (less than 5%, Table S1).

Table 4. Area, surface energy, and adsorption energy per unit area of O_2 for $CuFeS_2$ planes.

Planes	Area (nm^2)	Surface Energy, E_s ($J \cdot m^{-2}$)	Adsorption Site	Adsorption Energy per Unit Area ($kJ \cdot mol^{-1} \cdot nm^{-2}$)
112-S	0.473	0.923 [a]	S1	−437.384
112-M	0.473	1.018 [a]	Fe1	−1316.631
102	0.774	1.128 [a]	Fe1	−1372.095
			S3	−470.755
312-M	1.874	1.207 [a]	Fe1	−1571.115
312-S	1.874	1.221	S2	−477.523
110	0.408	1.332	Fe3	−1633.777
			S1	−461.095
116-S	0.909	1.351	S2	−527.396
116-M	0.909	1.494	Fe2	−1654.440
100-S	0.545	1.450	S3	−588.869
100-M	0.545	1.498	Fe3	−1858.123
001-S	0.274	1.495 [a]	S2	−690.193
001-M	0.274	1.566 [a]	Fe	−2027.415

[a] These data have been published in our previous research [27].

Since the leaching experiments were performed in a sulfuric acid solution at pH = 1, components such as H_2O, O_2, SO_4^{2-}, and HSO_4^- that could react with the $CuFeS_2$ planes were present in the solution. Research indicated that O_2 was adsorbed on the $CuFeS_2$ planes prior to the adsorption of H_2O, SO_4^{2-}, and HSO_4^- [27,34,35]. For example, de Lima et al. [34,45] reported that the adsorption energies were −142.12, −105.34, and 95.30 kJ·mol^{-1} for SO_4^{2-}, HSO_4^-, and H_2O at Fe sites on the $CuFeS_2$ (001) plane. Wei et al. [27] reported that the adsorption energies of H_2O and O_2 at Fe sites on the $CuFeS_2$ (001) plane were −153.94 and −556.12 kJ·mol^{-1}, respectively. In addition, the reactivity of the Fe sites was stronger than that of the Cu sites on the $CuFeS_2$ metal-terminated planes [27]. In this case, only the adsorption of O_2 at Fe and S sites on the $CuFeS_2$ planes was considered to compare the reactivity of each plane, and the results are shown in Table 4 and Figures 7 and S3.

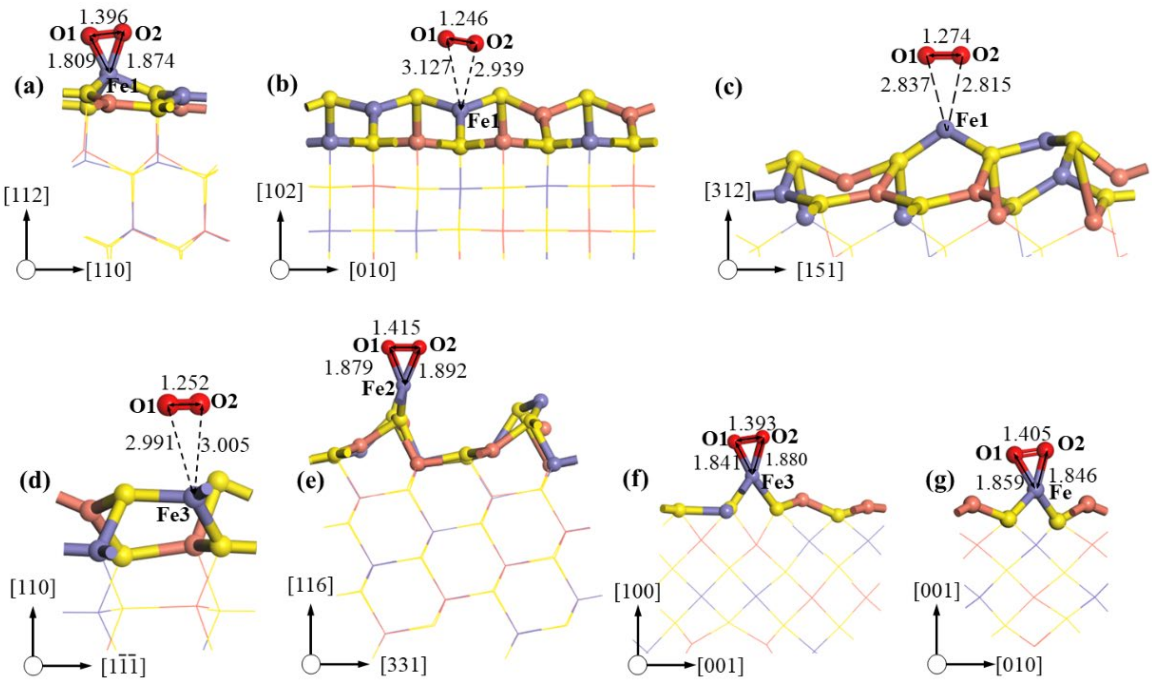

Figure 7. Layout of the adsorption of O_2 at Fe sites on $CuFeS_2$ planes: (**a**) (112)-M plane; (**b**) (102) plane; (**c**) (312)-M plane; (**d**) (110) plane; (**e**) (116)-M plane; (**f**) (100)-M plane; (**g**) (001)-M plane; distances are in Å.

It was clearly seen that the adsorption energy per unit area at Fe sites on each plane was more negative than that at S sites, suggesting that these Fe sites were more easily oxidized than the S sites due to the higher affinity of Fe sites for O_2 than that of S sites for O_2 [38]. For the adsorption of O_2 at Fe sites on $CuFeS_2$ planes, the adsorption energies per unit area were −1316.631, −1372.095, −1571.115, −1633.777, −1654.440, −1858.123, and −2027.415 kJ·mol^{-1}·nm^{-2} for the (112)-M, (102), (312)-M, (110), (116)-M, (100)-M, and (001)-M planes, respectively, suggesting that the Fe site of the $CuFeS_2$ (001) plane was more easily oxidized by O_2 than that in other planes [27,46], thereby forming two Fe-O bonds with lengths of 1.846 Å and 1.859 Å (Figure 7g). The adsorption energy per unit area of O_2 at S sites on the $CuFeS_2$ planes exhibited the same rules as that at Fe sites. The adsorption energies per unit area for the (112)-S, (102), (312)-S, (110), (116)-S, (100)-S, and (001)-S planes were −437.384, −470.755, −477.523, −461.095, −527.396, −588.869, and −690.193 kJ·mol^{-1}·nm^{-2}, respectively, suggesting that both the Fe and S sites of the $CuFeS_2$ (001) plane were more easily oxidized by O_2; thus, the (001) plane was preferably leached compared with other planes. Overall, the leaching rates of the $CuFeS_2$ planes were in the order of (001) > (100) > (116) > (110) > (312) > (102) > (112) planes.

In addition, it was clearly seen that the adsorption energies per unit area at Fe sites on the (001)-M and (100)-M planes were more negative than those on other planes (Figure 8a), while those on the (001)-S, (100)-S, and (116)-S planes were significantly more negative than those on other planes at the S sites (Figure 8b). In this case, the $CuFeS_2$ samples that contained more (001), (100), and (116) planes, exhibited faster leaching rates, consistent with the leaching experiment results, in which the Cu extraction was in the order of TM > RM > BM methods (Figure 1).

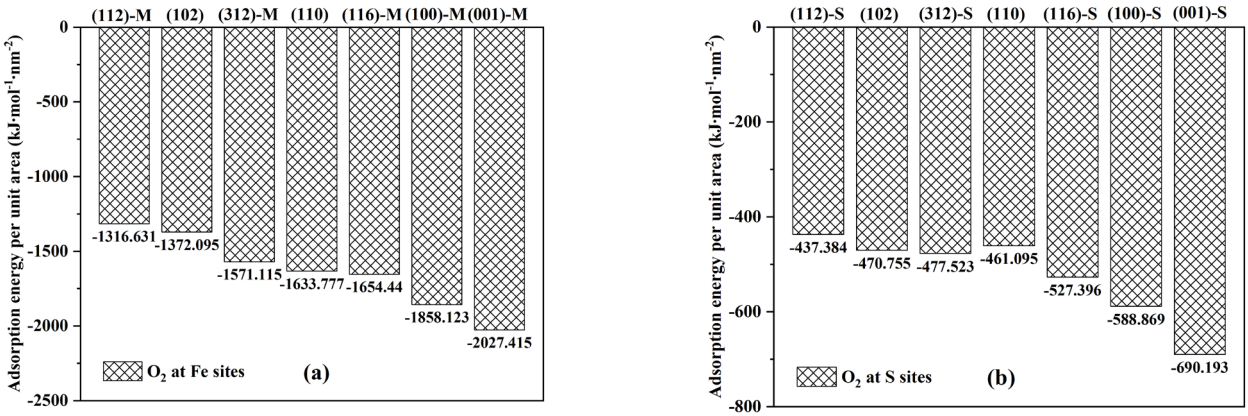

Figure 8. Adsorption energy per unit area for O_2 on $CuFeS_2$ planes: (**a**) Fe sites; (**b**) S sites.

4. Conclusions

In this work, a three-head laboratory mill with a grinder mill (TM), rod mill (RM), and ball mill (BM) was employed to obtain $CuFeS_2$ samples with anisotropic crystal planes. Interestingly, the trend of Cu extractions for three $CuFeS_2$ samples with a particle size of 38~75 μm increasing with leaching time were similar, while the Cu extractions were in the order of TM > RM > BM methods for the three $CuFeS_2$ samples with a particle size of 75~150 μm, indicating that the anisotropic crystal planes of $CuFeS_2$ particles could significantly affect $CuFeS_2$ leaching behavior. The exposed percentages of the $CuFeS_2$ planes were in the order of (112) > (102) > (312) > (110) > (116) > (100) > (001) planes, and the long, irregular particles obtained using the TM method exposed fewer (112), (102), (312), and (110) planes and more (116), (100), and (001) planes. Since the adsorption of O_2 on $CuFeS_2$ planes indicated that the leaching rates were in the order of (001) > (100) > (116) > (110) > (312) > (102) > (112) planes, $CuFeS_2$ samples treated using the TM method exhibited the highest oxidization degree. The formation of more SO_4^{2-} species indicated that $CuFeS_2$ samples treated using the TM method had the least amount of passivation layer, thus exhibiting the highest leaching rate.

Supplementary Materials: The following are available online at https://www.mdpi.com/article/10.3390/min13111461/s1: Figure S1. XRD patterns of raw $CuFeS_2$ sample (D8 Advance, Bruker, Germany). PDF: 71-0507 was the standard XRD pattern of $CuFeS_2$ from Jade 6.0. It was clear that the diffraction peaks of the raw chalcopyrite sample were highly consistent with the standard $CuFeS_2$ XRD pattern (PDF: 71-0507), indicating that the raw $CuFeS_2$ sample in this study was highly purified. Figure S2. Structure and exposed atoms of $CuFeS_2$ planes. Figure S3. Layout of the adsorption of O_2 at S sites on the $CuFeS_2$ planes: (a) (112)-S plane; (b) (102) plane; (c) (312)-S plane; (d) (110) plane; (e) (116)-S plane; (f) (100)-S plane; (g) (001)-S plane; distances are in Å. Table S1. Main element contents of $CuFeS_2$ sample using XRF (Zetium, PANalytical, Almelo, Netherlands) (wt. %). Table S2. Normalized exposure percentage of planes for standard and experimental $CuFeS_2$ particles (%). Table S3. Relatively normalized exposed percentage of planes for $CuFeS_2$ particles between standard value and experimental value (%).

Author Contributions: Software, Z.W.; writing—original draft, Z.W. and X.Y.; writing—review and editing, Y.L.; supervision, X.Y., W.L., Q.M., X.W. and Y.L. All authors have read and agreed to the published version of the manuscript.

Funding: The authors would like to acknowledge the financial support from the Key Research and Development Program of Hubei Province (2021BCA127).

Data Availability Statement: The data presented in this study are available on request from the corresponding author.

Conflicts of Interest: The authors declare no conflict of interest.

References

1. Jena, S.S.; Tripathy, S.K.; Mandre, N.R.; Venugopal, R.; Farrokhpay, S. Sustainable use of copper resources: Beneficiation of low-Grade copper ores. *Minerals* **2022**, *12*, 545.
2. Dutrizac, J.E. The kinetics of dissolution of chalcopyrite in ferric ion media. *Metall. Trans. B* **1978**, *9*, 431–439.
3. Córdoba, E.M.; Muoz, J.A.; Blázquez, M.L.; González, F.; Ballester, A. Leaching of chalcopyrite with ferric ion. Part I: General aspects. *Hydrometallurgy* **2008**, *93*, 81–87.
4. Li, W.Q.; Li, Y.B.; Wang, Z.H.; Yang, X.; Chen, W. Selective flotation of chalcopyrite from pyrite via seawater oxidation pretreatment. *Int. J. Min. Sci. Technol.* **2023**. [CrossRef]
5. Li, Y.B.; Kawashima, N.; Li, J.; Chandra, A.P.; Gerson, A.R. A review of the structure, and fundamental mechanisms and kinetics of the leaching of chalcopyrite. *Adv. Colloid Interface Sci.* **2013**, *197–198*, 1–32.
6. Moskalyk, R.R.; Alfantazi, A.M. Review of copper pyrometallurgical practice: Today and tomorrow. *Miner. Eng.* **2003**, *16*, 893–919.
7. Dimitrijević, M.; Kostov, A.; Tasić, V.; Milosević, N. Influence of pyrometallurgical copper production on the environment. *J. Hazard. Mater.* **2009**, *164*, 892–899. [CrossRef] [PubMed]
8. Savić, M.; Mihajlović, I.; Živković, Ž. An anfis–based air quality model for prediction of SO2 concentration in urban area. *Serbian J. Manag.* **2013**, *8*, 25–38.
9. Khoshkhoo, M.; Dopson, M.; Shchukarev, A.; Sandström, Å. Chalcopyrite leaching and bioleaching: An X-ray photoelectron spectroscopic (XPS) investigation on the nature of hindered dissolution. *Hydrometallurgy* **2014**, *149*, 220–227.
10. Watling, H.R. Chalcopyrite hydrometallurgy at atmospheric pressure: 1. Review of acidic sulfate, sulfate–chloride and sulfate–nitrate process options. *Hydrometallurgy* **2013**, *140*, 163–180.
11. Watling, H.R. Chalcopyrite hydrometallurgy at atmospheric pressure: 2. Review of acidic chloride process options. *Hydrometallurgy* **2014**, *146*, 96–110.
12. Nazari, G.; Dixon, D.G.; Dreisinger, D.B. The mechanism of chalcopyrite leaching in the presence of silver-enhanced pyrite in the galvanox™ process. *Hydrometallurgy* **2012**, *113–114*, 122–130. [CrossRef]
13. Hiroyoshi, N.; Arai, M.; Miki, H.; Tsunekawa, M.; Hirajima, T. A new reaction model for the catalytic effect of silver ions on chalcopyrite leaching in sulfuric acid solutions. *Hydrometallurgy* **2002**, *63*, 257–267. [CrossRef]
14. Pan, H.D.; Yang, H.Y.; Tong, L.L.; Zhong, C.B.; Zhao, Y.S. Control method of chalcopyrite passivation in bioleaching. *Trans. Nonferrous Met. Soc. China* **2012**, *22*, 2255–2260.
15. Tshilombo, A. Mechanism and Kinetics of Chalcopyrite Passivation and Depassivation during Ferric and Microbial Leaching. Ph.D. Thesis, University of British Columbia, Vancouver, BC, Canada, 2004.
16. Parker, A.; Klauber, C.; Kougianos, A.; Watling, H.R.; van Bronswijk, W. An X-ray photoelectron spectroscopy study of the mechanism of oxidative dissolution of chalcopyrite. *Hydrometallurgy* **2003**, *71*, 265–276. [CrossRef]
17. Harmer, S.L.; Pratt, A.R.; Nesbitt, W.H.; Fleet, M.E. Sulfur species at chalcopyrite (CuFeS2) fracture surfaces. *Am. Mineral.* **2004**, *89*, 1026–1032. [CrossRef]
18. Klauber, C.; Parker, A.; van Bronswijk, W.; Watling, H. Sulphur speciation of leached chalcopyrite surfaces as determined by X-ray photoelectron spectroscopy. *Int. J. Miner. Process.* **2001**, *62*, 65–94. [CrossRef]
19. Córdoba, E.M.; Muñoz, J.A.; Blázquez, M.L.; González, F.; Ballester, A. Passivation of chalcopyrite during its chemical leaching with ferric ion at 68 °C. *Miner. Eng.* **2009**, *22*, 229–235. [CrossRef]
20. Viramontes-Gamboa, G.; Peña-Gomar, M.M.; Dixon, D.G. Electrochemical hysteresis and bistability in chalcopyrite passivation. *Hydrometallurgy* **2010**, *105*, 140–147. [CrossRef]
21. Li, J.; Kawashima, N.; Kaplun, K.; Absolon, V.J.; Gerson, A.R. Chalcopyrite leaching: The rate controlling factors. *Geochim. Cosmochim. Acta* **2010**, *74*, 2881–2893. [CrossRef]
22. Parker, G.K.; Woods, R.; Hope, G.A. Raman investigation of chalcopyrite oxidation. *Colloids Surf. A Physicochem. Eng. Asp.* **2008**, *318*, 160–168. [CrossRef]
23. Ciobanu, C.L.; Cook, N.J.; Ehrig, K. Ore minerals down to the nanoscale: Cu-(Fe)-sulphides from the iron oxide copper gold deposit at Olympic Dam, South Australia. *Ore Geol. Rev.* **2017**, *81*, 1218–1235. [CrossRef]
24. Harmer, S.L.; Thomas, J.E.; Fornasiero, D.; Gerson, A.R. The evolution of surface layers formed during chalcopyrite leaching. *Geochim. Cosmochim. Acta* **2006**, *70*, 4392–4402. [CrossRef]
25. Khoshkhoo, M.; Dopson, M.; Engström, F.; Sandström, Å. New insights into the influence of redox potential on chalcopyrite leaching behaviour. *Miner. Eng.* **2017**, *100*, 9–16. [CrossRef]
26. Wei, Z.L.; Li, Y.B.; Huang, L.Y. New insight into the anisotropic property and wettability of molybdenite: A DFT study. *Miner. Eng.* **2021**, *170*, 107058. [CrossRef]

27. Wei, Z.L.; Li, Y.B.; Gao, H.M.; Zhu, Y.G.; Qian, G.J.; Yao, J. New insights into the surface relaxation and oxidation of chalcopyrite exposed to O2 and H2O: A first-principles DFT study. *Appl. Surf. Sci.* **2019**, *492*, 89–98. [CrossRef]
28. Majuste, D.; Ciminelli, V.S.T.; Eng, P.J.; Osseo-Asare, K. Applications of in situ synchrotron XRD in hydrometallurgy: Literature review and investigation of chalcopyrite dissolution. *Hydrometallurgy* **2013**, *131*, 54–66. [CrossRef]
29. Xie, H.Y.; Su, X.L.; Zheng, G.; Yan, Y.G.; Liu, W.; Tang, H.; Kanatzidis, M.G.; Uher, C.; Tang, X.F. Nonmagnetic in substituted CuFe1–xInxS2 solid solution thermoelectric. *J. Phys. Chem. C* **2016**, *120*, 27895–27902. [CrossRef]
30. Zhang, Y.; Zhao, G.G.; Lv, X.; Tian, Y.; Yang, L.; Zou, G.Q.; Hou, H.S.; Zhao, H.B.; Ji, X.B. Exploration and size engineering from natural chalcopyrite to high-performance electrode materials for lithium-ion batteries. *ACS Appl. Mater. Interfaces* **2019**, *11*, 6154–6165. [CrossRef]
31. de Oliveira, C.; de Lima, G.F.; de Abreu, H.A.; Duarte, H.A. Reconstruction of the chalcopyrite surfaces—A DFT study. *J. Phys. Chem. C* **2012**, *116*, 6357–6366. [CrossRef]
32. Zhou, X.; Liu, D.; Bu, H.; Deng, L.; Liu, H.; Yuan, P.; Du, P.; Song, H. Xrd-based quantitative analysis of clay minerals using reference intensity ratios, mineral intensity factors, rietveld, and full pattern summation methods: A critical review. *Solid Earth Sci.* **2018**, *3*, 16–29. [CrossRef]
33. Hu, Y.H.; Gao, Z.Y.; Sun, W.; Liu, X.W. Anisotropic surface energies and adsorption behaviors of scheelite crystal. *Colloids Surf. A Physicochem. Eng. Asp.* **2012**, *415*, 439–448. [CrossRef]
34. de Lima, G.F.; de Oliveira, C.; de Abreu, H.A.; Duarte, H.A. Sulfuric and hydrochloric acid adsorption on the reconstructed sulfur terminated (001) chalcopyrite surface. *Int. J. Quantum Chem.* **2012**, *112*, 3216–3222. [CrossRef]
35. Sokic, M.D.; Markovic, B.; Zivkovic, D. Kinetics of chalcopyrite leaching by sodium nitrate in sulphuric acid. *Hydrometallurgy* **2009**, *95*, 273–279. [CrossRef]
36. Gao, Z.Y.; Li, C.W.; Sun, W.; Hu, Y.H. Anisotropic surface properties of calcite: A consideration of surface broken bonds. *Colloids Surf. A Physicochem. Eng. Asp.* **2017**, *520*, 53–61. [CrossRef]
37. Moimane, T.; Plackowski, C.; Peng, Y.J. The critical degree of mineral surface oxidation in copper sulphide flotation. *Miner. Eng.* **2020**, *145*, 106075. [CrossRef]
38. Li, Y.B.; Chandra, A.P.; Gerson, A.R. Scanning photoelectron microscopy studies of freshly fractured chalcopyrite exposed to O2 and H2O. *Geochim. Cosmochim. Acta* **2014**, *133*, 372–386. [CrossRef]
39. Zhang, P.; Huang, W.; Ji, Z.; Zhou, C.G.; Yuan, S.H. Mechanisms of hydroxyl radicals production from pyrite oxidation by hydrogen peroxide: Surface versus aqueous reactions. *Geochim. Cosmochim. Acta* **2018**, *238*, 394–410. [CrossRef]
40. Khoso, S.A.; Hu, Y.H.; Lu, F.; Gao, Y.; Liu, R.Q.; Sun, W. Xanthate interaction and flotation separation of H2O2-treated chalcopyrite and pyrite. *Trans. Nonferrous Met. Soc. China* **2019**, *29*, 2604–2614. [CrossRef]
41. Li, Y.B.; Wei, Z.L.; Xiao, Q.; Gao, H.M.; Song, S.X. A fundamental DFT study of chalcopyrite surface evolution due to impurity divalent ions during leaching process. *Miner. Eng.* **2018**, *121*, 205–211. [CrossRef]
42. Silva, J.C.M.; Abreu, H.A.D.; Duarte, H.A. Electronic and structural properties of bulk arsenopyrite and its cleavage surfaces—A DFT study. *Rsc Adv.* **2014**, *5*, 2013–2023. [CrossRef]
43. Hung, A.; Muscat, J.; Yarovsky, I.; Russo, S.P. Density-functional theory studies of pyrite FeS2 (100) and (110) surfaces. *Surf. Sci.* **2002**, *513*, 511–524. [CrossRef]
44. Hung, A.; Muscat, J.; Yarovsky, I.; Russo, S.P. Density-functional theory studies of pyrite FeS2 (111) and (210) surfaces. *Surf. Sci.* **2002**, *520*, 111–119. [CrossRef]
45. de Lima, G.F.; de Oliveira, C.; de Abreu, H.A.; Duarte, H.A. Water adsorption on the reconstructed (001) chalcopyrite surfaces. *J. Phys. Chem. C* **2011**, *115*, 10709–10717. [CrossRef]
46. Xiong, X.L.; Hua, X.M.; Zheng, Y.F.; Lu, X.G.; Li, S.G.; Cheng, H.W.; Xu, Q. Oxidation mechanism of chalcopyrite revealed by X-ray photoelectron spectroscopy and first principles studies. *Appl. Surf. Sci.* **2018**, *427*, 233–241. [CrossRef]